Journal of Materials Chemistry A

ROYAL SOCIETY OF CHEMISTRY

PAPER

View Article Online
View Journal | View Issue

Cite this: J. Mater. Chem. A, 2023, 11, 8110

A dual-functional device based on CB/PVDF@BFP for solar-driven water purification and water-induced electricity generation†

Jiangchao Huang,‡[a] Veronica Pereira,‡[b] Chenyue Wang,‡[a] Haitao Li,*[a] Hiang Kwee Lee *[bc] and Jie Han *[a]

The efficient utilization of low-grade thermal energy to produce clean water or electricity is important because it potentially relieves our demand on limited natural water and energy resources. Here, we propose a dual-functional device to couple solar-driven water evaporation and evaporation-induced power generation for concurrent production of clean water and green electricity. Our strategy involves the fabrication of an asymmetric, dual-layered structure by spraying a carbon black/polyvinylidene fluoride mixture onto bamboo filter paper (CB/PVDF@BFP). The upper CB/PVDF layer serves as a light-to-thermal transducer for instantaneous heating, while the bottom BFP layer functions as a hydrophilic porous platform to boost water uptake and transfer. Moreover, water evaporation drives capillary flow of ions on the conductive CB/PVDF layer to create a pseudostream that can be harnessed for power generation. Notably, our dual-functional device delivers a fast water evaporation rate of 1.44 kg m^{-2} h^{-1} and a high energy utilization rate of 92% under one sun, beyond the previous carbon-based reports. Through this solar-driven water evaporation process, we achieve the efficient desalination of artificial seawater and decontamination of organic-polluted water by up to 99.8% and nearly 100%, respectively. Our device also concurrently produces high, consistent evaporation-induced electrical outputs with V_{OC} and I_{SC} of 0.32 V and 1.5 μA, respectively. The generated electrical outputs can be easily stored by charging a capacitor to over 1.5 V within 15 minutes and be subsequently utilized on demand to power common household electronics. By enabling the efficient coupling of multiple solar-driven processes, our work will catalyze the design of next-generation multifunctional devices to ensure electricity and potable water are easily accessible by everyone, especially remote areas without power stations and/or water treatment facilities.

Received 3rd January 2023
Accepted 20th February 2023

DOI: 10.1039/d3ta00032j

rsc.li/materials-a

1. Introduction

The rapid growth of the global economy and population imposes an ever-increasing demand on the Earth's limited water and energy resources. At present, the shortages of clean water and energy are two inevitable challenges facing the sustainable development of human civilization.[1–3] To address these issues, major research efforts have been directed to exploit widely abundant sunlight for (sea)water treatment/purification[4–6] and green energy generation.[7–10] Notably, solar-driven water evaporation[11] and evaporation-induced electrical power generation[12] are two emerging approaches that exploit sunlight to produce clean water and green electricity, respectively.[13,14] On the one hand, solar-driven water evaporation involves the conversion of solar energy into thermal energy[15–17] to generate steam for the subsequent collection as clean water. On the other hand, evaporation-driven power generation employs the water evaporation process to produce a pseudostreaming current[18–20] for autonomous sunlight-to-electricity transformation. These two technologies are immensely attractive for the decentralized production of clean water and green electricity with potential widespread applicability.

Despite their huge promises in solar-driven water purification and power generation applications, current designs suffer several drawbacks which limit their practical applications. For instance, conventional methods for solar-driven water evaporation typically involve the use of carbon-based materials on hydrophilic sponges for photothermal heating and water transportation. However, the water evaporation process is impeded by poor light absorption as well as low heat

[a]School of Chemistry and Chemical Engineering, Yangzhou University, Yangzhou, 225002, PR China. E-mail: htli@yzu.edu.cn; hanjie@yzu.edu.cn
[b]Division of Chemistry and Biological Chemistry, School of Chemistry, Chemical Engineering and Biotechnology, Nanyang Technological University, 21 Nanyang Link, 637371, Singapore. E-mail: hiangkwee@ntu.edu.sg
[c]Institute of Materials Research and Engineering, The Agency for Science, Technology and Research (A*STAR), 2 Fusionopolis Way, #08-03, Innovis, 138634, Singapore

† Electronic supplementary information (ESI) available. See DOI: https://doi.org/10.1039/d3ta00032j

‡ These authors contributed equally to this work.

conversion[21–24] efficiency arising from rapid heat dissipation *via* non-evaporative mechanisms, such as heat conduction[25–27] into the bulk water or the supporting medium. It is also noteworthy that the evaporation process accumulates salt[27–31] in the device, thereby hindering efficient water transportation and corresponding solar-to-vapor efficiency. More importantly, current solar-driven water evaporation devices[32–34] and evaporation-induced power generators[35–37] have only a single function to either produce potable water or electricity, respectively. While these evaporation-driven concepts are complementary, there is a lack of report demonstrating their facile integration to simultaneously harness green electricity and clean water during water evaporation.

Herein, we realize the parallel production of clean water and green energy by introducing an efficient, dual-functional device to effectively couple the two evaporation-driven processes. The device is easily fabricated by spraying a carbon black/polyvinylidene fluoride mixture onto bamboo filter paper (CB/PVDF@BFP). Our design comprises of two key components. (1) An upper CB/PVDF layer with broadband light absorption and high photothermal conversion. This solar-thermal layer heats upon light irradiation to evaporate water, and doubles as a hydrophobic platform to inhibit salt accumulation. (2) A bottom bamboo filter paper serving as a hydrophilic layer to enhance water uptake and transportation across the device. Our asymmetric hydrophilic/hydrophobic dual-layer platform is crucial to boost steam generation and harvest electricity from the pseudostreaming current during water evaporation.

Notably, our dual-functional device delivers a fast water evaporation rate of 1.44 kg m^{-2} h^{-1} and a high energy utilization rate of 92% under one sun irradiation, excelling over other carbon-based designs. Using this device, we achieve the efficient desalination of artificial seawater and decontamination of organic-polluted water up to 99.8% and nearly 100% efficiencies, respectively. Our device also concurrently produces high, consistent evaporation-induced electrical outputs with V_{OC} and I_{SC} of 0.32 V and 1.5 μA, respectively. The generated electrical outputs can be easily stored by charging a capacitor to more than 1.5 V within 15 minutes and released on-demand to power common household electronics, such as an LCD thermostat. Our work on a Janus-like bifunctional device offers valuable insights on the design of next-generation multifunctional devices for simultaneous, decentralized production of green energy and clean water using sunlight as a renewable energy source.

2. Experimental section

2.1 Materials

Polyvinylidene fluoride (PVDF, MW = 900 000), acetone (99%), anhydrous ethanol (99%), and carbon black powders (CB with 1000, 2000, 3000, 4000, 4500, and 5000 mesh, which are denoted as CB-1, CB-2, CB-3, CB-4, CB-5, and CB-6, respectively) were purchased from Shanghai Aladdin Biochemical Technology Co., Ltd. All chemicals were of analytical grade and used without further purification. Glass spray bottles (20 mL), glass cover, resistance package (1–7500 KΩ), and other conductive materials were purchased from an online store (Tmall supermarket).

2.2 Preparation of CB/PVDF@BFP

CB with 4500 mesh was selected for the preparation of a carbon black/polyvinylidene fluoride mixture onto bamboo filter paper (CB/PVDF@BFP). PVDF (0.12 g) was first dispersed in acetone (6.0 mL) and anhydrous ethanol (9.2 mL). The solution was stirred using a magnetic stirrer till it became transparent. 45% CB was then added, ultrasonicated and mixed evenly to obtain the sprayable precursor solution. The as-obtained solution was subsequently sprayed on a BFP (70 × 160 × 0.35 mm^3) and dried under ambient conditions. CB/PVDF@BFP was then cut into rectangular pieces (30 × 70 mm^2) for subsequent experiments on solar-driven water purification and evaporation-induced electricity generation.

2.3 Construction of the dual-functional device

Four evaporation-induced power generators and evaporative materials were inserted in series into the water reservoir. The upper and lower ends of the materials were then connected with wires in series and the entire device was covered in a glass cover to obtain a dual-functional device for solar evaporation and evaporation-induced power generation. The dual-functional device was also connected with a digital ammeter to quantify real-time current, and voltage obtained under simulated sunlight irradiation. The condensate was also concurrently collected as clean water.

2.4 Characterization of the dual functional device

The morphology and surface structures of BFP and CB/PVDF@BFP were characterized by scanning electron microscopy (SEM). SEM is a Zeiss field emission scanning electron microscope, which works at an accelerating voltage of 5 kV. The surface functional groups and chemical bond valence states were analyzed by Fourier transform infrared spectroscopy (FT-IR), and the surface temperature of the material was measured using an infrared thermal imager (FLIR). A UV visible near infrared absorption spectrometer (UV-Vis-NIR, Cary 5000, Agilent Technologies Inc., USA) was used to measure the absorbance of BFP and CB/PVDF@BFP in the wavelength range of 200–2500 nm. The CB was qualitatively analyzed using a powder X-ray diffractometer (from the Brooke company in Germany) at an angle range of 10–80°. The wettability and tensile stress of different materials were evaluated by the contact angle (WCA) measurement test and tensile test, respectively.

2.5 Solar-driven water purification and solar steam generation experiments

The surface of the porous carbon membrane was characterized as negatively charged using zeta potential measurement. The abundance of negatively charged surface functional groups allows the repulsion of hydroxyl ions in water to allow for their subsequent flow and to create a high potential downstream.

This phenomenon will create a potential difference between the upper and lower ends, thereby generating current.

A simulated solar irradiation lamp with a standard AM 1.5 g spectrum was used to study the evaporation performance of water. During the evaporation experiment, an electronic balance (Leqi) was used to record the mass change of deionized water with an accuracy of 0.001 g. The surface temperature was monitored using an infrared thermal imager (FILR). Inductively coupled plasma mass spectrometry (PerkinElmer optima 7300 DV) was employed to analyze the ion concentration of seawater before and after evaporation. The photothermal conversion efficiency was calculated using the following formula:

$$\eta = \dot{m}h_{LV}/C_{opt}q_i$$

where $\dot{m}$ is the evaporation rate under different illumination conditions, subtracting the contributions from the intrinsic evaporation rate in the dark and by the support. h_{LV} represents the evaporation enthalpy, including both the sensible and latent heat of the phase change, C_{opt} is the optical concentration and q_i is the standard solar radiation.

3. Results and discussion

We chose BFP as the device's base material because it contains an abundance of hydrophilic fibers to promote water uptake and transfer *via* strong capillary forces for enhanced steam generation. Moreover, we use carbon black (CB) and polyvinylidene fluoride (PVDF) in our design due to two main reasons. (1) CB is a cost-effective and readily available commercial product that functions as both an efficient photothermal and electroactive material. These two properties are in turn important for efficient light-to-heat conversion, as well as to create pseudopotential for power generation. (2) PVDF possesses excellent hydrophobic properties (*e.g.*, it serves as the hydrophobic layer in a Janus structure) and adhesive property, and is easily formed. These factors are crucial for the spray fabrication of functional PVDF film. Hence, both the CB and PVDF are key material components necessary for the fabrication of our device in the current study.

We affirm the chemical and physical integrities of the CB powder using XRD, FT-IR, particle size analyzer, and XPS characterizations (Fig. S1–3†). The XRD pattern indicates that the larger CB particles (4500 and 5000 mesh) demonstrate the amorphous nature of the solid, which lacks long-term crystalline order and primarily consists of sp^2 and sp^3 bonding. In contrast, the smaller CB particles (1000–3000 mesh, lower photothermal temperature) exhibit a typical graphited crystal structure, which may be derived from a small composition of graphitic crystallites in the carbon black samples. This is due to the reflectivity of graphite being higher than that of pure carbon black. Moreover, amorphous CB powders contain numerous loosely held π electrons from the electron-donating group (CO group) which will facilitate broadband light absorption, as confirmed by FTIR and XPS measurements.

To prepare our device, we adopt a unique sprayable process to selectively coat the CB/PVDF composite on one side of BFP. Notably, this preparation process enables the CB/PVDF mixture to partially penetrate the BFP, thereby creating an asymmetric dual-layer structure with no gaps between the upper hydrophobic CB/PVDF and bottom hydrophilic BFP layers. The absence of a void in the Janus-like device is crucial to facilitate water and heat transfer, and also to reduce the device's thermal conductivity for heat localization (Fig. 1a). Upon sunlight irradiation, our design will rapidly evaporate seawater while the hydrophilic BFP layer continuously supplies seawater to the solar-thermal layer. We anticipate two key processes necessary for concurrent current generation (Fig. 1b). (1) Hydrogen ions in seawater are attracted strongly to the negatively charged CB/PVDF@BFP surface as it passes through the nanochannel, thereby forming an electric double layer. (2) Hydroxyl anions migrate in a unidirectional path with the water flow to generate current and form a moving potential. As a proof-of-concept application, we will subsequently realize a solar-driven, dual-functional device for parallel (sea)water purification and evaporation-induced power generation (Fig. 1c).

To affirm the successful loading of CB/PVDF on BFP, we characterize the CB/PVDF@BFP ensemble using SEM and elemental techniques. As shown in Fig. 2a and b, CB/PVDF@BFP has a layered nanostructure comprising of rough

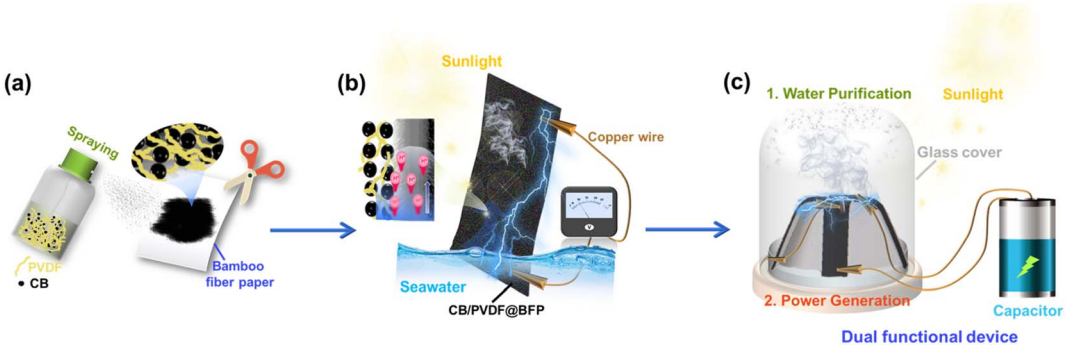

Fig. 1 Schematic illustrations of the interfacial evaporation system based on CB/PVDF@BFP for solar-driven water purification and evaporation-induced electricity generation. (a) Preparation process of the CB/PVDF@BFP material. (b) Working principles of the water purification and evaporation-induced power generation processes on the CB/PVDF@BFP platform upon sunlight irradiation. (c) Dual-functional device for concurrent solar-driven water purification and power generation.

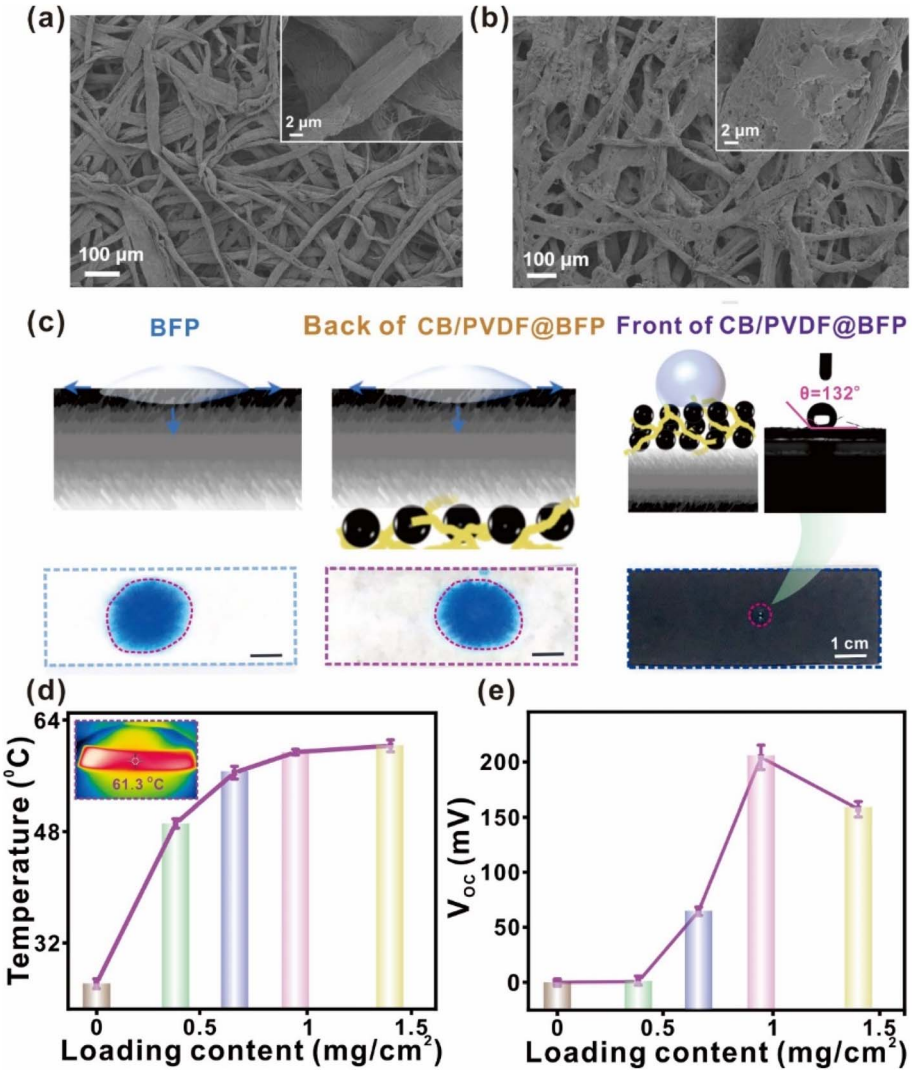

Fig. 2 Optimization of the CB/PVDF@BFP platform. SEM images of the surface of (a) BFP and (b) CB/PVDF@BFP. (c) Water contact angle images when a water droplet is placed on BFP (left), as well as the back (middle) and front (right) of the CB/PVDF@BFP platform. (d) Photothermal temperature and (e) V_{OC} of the CB/PVDF@BFP platform at different mass loading under 1 sun irradiation and 25 °C.

BFP carbon fibers that are uniformly loaded with the CB/PVDF, as demonstrated by EDS analysis (Fig. S4–6†). The hierarchical nanoscale feature and microscale pores notably facilitate effective sunlight absorption and steam evaporation, respectively. The high CB loading ensures good long-term thermal conductivity and efficient solar energy absorption, whereas the PVDF binder aids in film formation and enhances the stability of the CB/PVDF@BFP ensemble. Notably, the effective integration of the hydrophilic and hydrophobic layers with no gap is crucial to ensure continuous water supply for both steam generation and evaporation-driven power generation.

The asymmetric dual-layer design with an upper hydrophobic CB/PVDF layer and bottom hydrophilic BFP support is important for our target solar-driven applications. We thus evaluate the wettability of the front and back surfaces of the CB/PVDF@BFP ensemble using aqueous dye solutions and sessile water droplets. As shown in Fig. 2c, 0.5 mL methylene blue (MB; 0.04 mg mL^{-1}) dye was added to the surface of the material. Notably, the BFP and backside of CB/PVDF@BFP (*i.e.*, with BFP exposed to the solution) exhibit high wettability, as evident from the instantaneous spreading and absorption of MB solution into the porous material. This hydrophilicity is conducive for rapid water transportation through the porous channels. In contrast, the front of the CB/PVDF@BFP ensemble is hydrophobic and demonstrates a large water contact angle of 132°. Moreover, tensile stress measurements highlight that the loading of CB/PVDF (Fig. S7†) onto the BFP improves the mechanical properties of the ensemble, a key criterion to obtain a robust device for subsequent applications.

We further optimize the CB/PVDF@BFP platform by studying the heat conversion and evaporation-induced power generation performances at various areal loadings of the photothermal-active material (*i.e.*, CB). The comprehensive investigations highlight three important observations. (1) We optimize CB at 4500 mesh because it possesses the best photothermal conversion and evaporation-induced power

generation performances compared to other sizes (1000–5000 mesh; Fig. S8 and 9†). This observation can be attributed to the following two reasons. (i) Compared with the CB with 4500 mesh, the CB with mesh sizes from 1000 to 3000 possess more graphite-like crystallites, as confirmed by XRD (in Fig. S1†). These graphite-like crystallites have higher reflectivity which decreases their light absorption performance[38] and weaken subsequent photothermal conversions. (ii) The CB with 4500 mesh has better hydrophilicity as compared to the others (Fig. S8†), which is more favorable for the interactions between water molecules and CB's surface for power generation. (2) Increasing the areal loading density of the photothermal material results in enhanced solar light absorption, thereby boosting photothermal conversion (Fig. S10†). Together with the longer effective incident light path enabled by its unique layered design, the better light–matter interactions of CB/PVDF@BFP notably raises the equilibrium surface temperature to a maximum of ~62 °C at an area loading of 1.0 mg cm^{-2} (Fig. 2d). It should be noted that when the surface loading of the CB/PVDF composite is above 1.0 mg cm^{-2}, overloading of the composite will hinder the water transmission and cause a reduction of internal resistance.[12,39] Such undesired factors will weaken the electrical power generation. Hence, we optimize the areal loading at 1.0 mg cm^{-2} owing to its best photothermal performance. (3) An increase in CB/PVDF loading density boosts electrical power generation, reaching an optimal open-circuit voltage (V_{OC}) and short-circuit current (I_{SC}) of 0.21 V and 1.3 μA (Fig. 2e and S12a†), respectively. The enhanced power generation is attributed to an increase in the negative surface charges with more CB/PVDF loading, and the power generation mechanism is discussed in detail, as shown in Fig. S11.† Consequently, a larger concentration gradient of hydroxyl ions can be created at opposite ends of the device to generate higher electrical outputs.

In addition to the areal loading density of CB/PVDF, we also investigate the effects of other factors (*i.e.*, material length and width, and types of liquid used) on CB/PVDF@BFP's power generation. To monitor the potential difference created in real time, we first connect the opposite ends of the device to a digital current voltmeter (Fig. 3a) and selectively dispense different aqueous/organic solutions on one end of the device. We first observed that the V_{OC} and I_{SC} of CB/PVDF@BFP initially increased with the device length, reaching the highest values of 0.25 V and 1.45 μA at an optimal length of 7 cm (Fig. 3b and S12b†). The observed drop in electrical voltage after 7 cm is likely due to the reduced amount of evaporation at the other end of the device for efficient current generation. It is also noteworthy that a change in the device width affects the V_{OC} and I_{SC} of the material, whereby a width of 3 cm gives the maximum electrical outputs of 0.32 V and 1.6 μA (Fig. 3c and S12c†). This can be attributed to the fact that the number of mobile ions increases with the increase of width, but the current voltage decreases after 3 cm. This is because further widening of the CB/PVDF@BFP platform beyond 3 cm will affect water transportation and shorten the capillary wetting zone, thereby decreasing the current output.[40] More importantly, comprehensive investigations into the effect of different test solutions (C_2H_5OH, methyl orange (MO), methylene blue (MB), H_2O, and seawater) underscore the importance of ions to drive power generation (Fig. 3d and S12d†). For instance, an increase in the salt concentration renders the brine solution with higher conductivity to reduce the devices' electrical resistance and provide more mobile ions for current generation. This phenomenon thus induces a large concentration difference between opposite ends of the device to generate a V_{OC} and I_{SC} of 0.45 V and 2.3 μA (Fig. S13†), respectively.

Notably, the CB/PVDF@BFP's electrical outputs are easily modulated by connecting the platforms in series and/or with

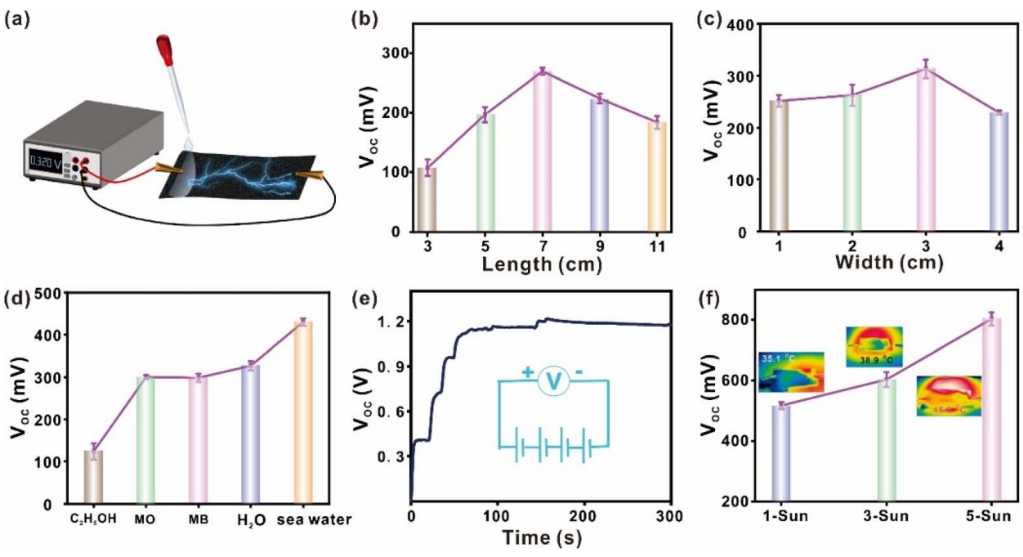

Fig. 3 Evaporation-induced electricity generation by the CB/PVDF@BFP platform. (a) Scheme depicting the experimental setup to characterize power generation performance. V_{OC} of the CB/PVDF@BFP platform at various device (b) length, (c) width, and (d) when subjected to different liquids/solutions under 1 sun and 25 °C. (e) V_{OC} of CB/PVDF@BFP platforms that are connected in series under 1 sun or (f) under different sunlight intensities (1–5 sun) at 25 °C. Insets: IR images.

the use of stronger sunlight irradiation power. For instance, we can attain an overall V_{OC} of 1.2 V (Fig. 3e) by connecting four CB/PVDF@BFP platforms in series and adding deionized water to one end of each platform. Similarly, the I_{SC} also rises to ~5 μA when the CB/PVDF@BFP platforms are connected in parallel (Fig. S14†). Moreover, we also observe an increase in both the device V_{OC} and I_{SC} when we gradually raise the solar irradiation power from 1 to 5 sun (Fig. 3f). This observation is attributed to the corresponding increase in photothermal temperature at higher solar intensity. Such increase of the platform temperature promotes faster water evaporation and transfer within the device, thereby accelerating ion flow to generate higher electrical output.

Furthermore, we have evaluated the device's maximum output power under different operation conditions (Fig. S15†). Fig. S15a† shows that when our device is subjected to a solution containing increasing NaCl concentrations (0.8–20%), the maximal output power for the CB/PVDF@BFP platform (load resistance: 2 MΩ) increases with the NaCl concentrations from 390 to 793 nW. Such improvement of power output with NaCl concentration is attributed to the reduction in the material's resistance and an increase in ion concentration for the generation of pseudostreaming current. Moreover, the maximum output power also increases from 800 to 1571 nW when we increase solar irradiation power from 1 to 5 sun, respectively. The increase in power output arises from the increase in evaporation rate under stronger sun irradiance, whereby the rapid evaporation of water facilitates ion flow to generate higher electrical output.

Solar-driven water evaporation offers enormous opportunities for decentralized water purification using sunlight as a renewable energy source. As a proof-of-concept demonstration, we designed a solar-driven device to desalinate seawater and treat wastewater for clean water production, as shown in Fig. 4a. The CB/PVDF@BFP is first incorporated onto a BFP foam which serves as a flotation platform to help position our device on the water surface. The BFP foam also aids in the absorption of water to constantly supply water for evaporation. We first evaluate the CB/PVDF@BFP platform for its steam generation properties. Notably, the CB/PVDF@BFP affords a rapid water evaporation rate and evaporation efficiency of 1.44 kg m^{-2} h^{-1} and ~92% (Fig. 4b), respectively, under sunlight irradiation at 1 kW m^{-2}, which are higher than those of previous carbon-based devices (Table S1†).[17,32,41–45] CB/PVDF@BFP under light irradiation also exhibits solar-thermal evaporation performances that are ~15 and 4-fold higher than the use of CB/PVDF@BFP in the dark (0.1 kg m^{-2} h^{-1}) and BFP only (0.4 kg m^{-2} h^{-1}) under similar one-sun illumination, respectively. We also note that an increase in solar irradiation power (*i.e.*, from 1 to 5 sun) promotes solar steam generation due to the higher photothermal heat generated by the CB/PVDF/BFP platform (Fig. S16†). These findings clearly affirm the importance of the CB/PVDF photothermal layer and sunlight in driving efficient solar-driven steam generation.

Having established its superior photothermal steam generation, we further apply CB/PVDF@BFP for solar-driven seawater desalination and water purification. For the solar desalination experiment, we investigate four artificial seawater samples with salinities representing those of the Baltic Sea (lowest salinity, 0.8 wt%), world ocean (3.5 wt%), the Red Sea (4 wt%), as well as a saturated salt solution (20 wt%). This was mainly to study the influence of high salt concentration on the evaporation rate of

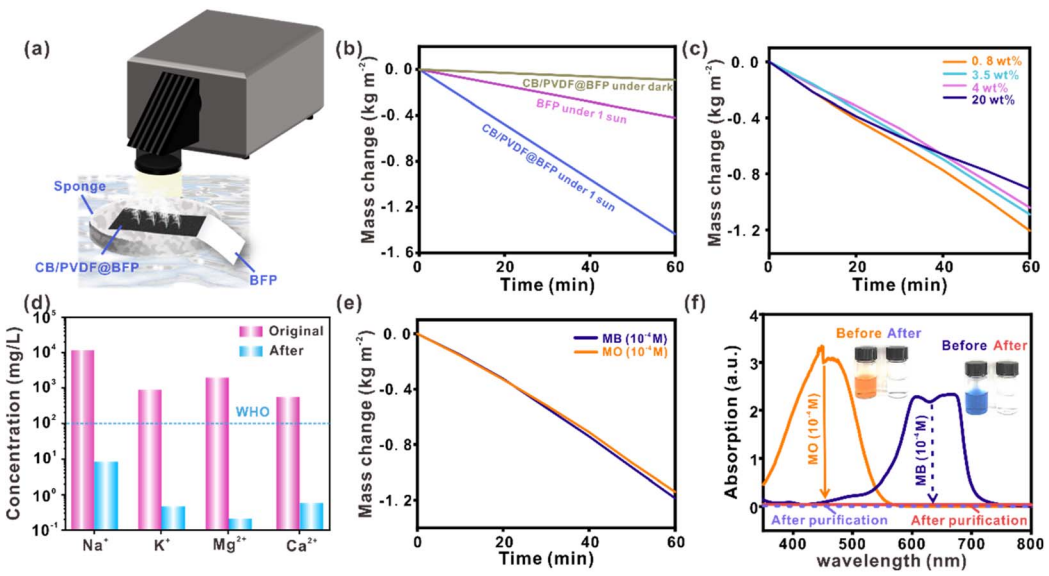

Fig. 4 Solar-driven water purification of CB/PVDF@BFP. (a) Scheme depicting the experimental setup for solar-driven water purification. Mass change of water for the experiment performed using different (b) experimental conditions and (c) artificial seawater samples at different salt concentrations. (d) Concentrations of various ionic species in the seawater and condensate collected after solar thermal desalination. WHO refers to the standard set by World Health Organization (WHO). (e) Application of CB/PVDF@BFP for solar steam generation to treat water contaminated with organic pollutants, such as methyl orange (MO) and methylene blue (MB). (f) UV-vis absorption spectra of water contaminated with MO and MB dyes, as well as the collected condensate from the steam generation.

CB/PVDF@BFP, with the aim to determine the resistance of various materials to salt accumulation. The photothermal evaporation rates of the four seawater samples are rather similar at 1.206 kg m^{-2} h^{-1}, 1.090 kg m^{-2} h^{-1}, 1.042 kg m^{-2} h^{-1}, and 0.908 kg m^{-2} h^{-1}, respectively. More importantly, the condensate collected from the solar desalination process is clean whereby the concentrations of Na^+, Mg^{2+}, K^+ and Ca^{2+} are reduced drastically by 2–3 orders of magnitude (Fig. 4d), signifying a high desalination efficiency of ~99.8% (Fig. S17†). It is worth noting that the quality of collected clean water is significantly better than the standards set by the World Health Organization (WHO) and the United States Environmental Protection Agency (EPA). With increasing salt concentrations, only a small amount of salt is observed to accumulate on the CB/PVDF@BFP surface even when desalinating a 20% salt solution. When the light is switched off, the accumulated salt dissolves completely to regenerate the platform for subsequent desalination cycles while maintaining its high intrinsic evaporation rates. Our CB/PVDF@BFP platform exhibits strong resistance towards salt accumulation due to the hydrophobic–hydrophilic dual-layer design (Fig. S18†), thereby addressing the usual formation of salt crystals in conventional hydrophilic platforms. In addition, the CB/PVDF@BFP device also maintains a high photothermal evaporation rate of ≥1.140 kg m^{-2} h^{-1} when employed for the treatment of water contaminated by common organic pollutants (Fig. 4e and S19†), such as methylene blue (MB) and methyl orange (MO) dyes at 10^{-4} to 10^{-5} M. The water obtained after the solar-driven purification process is clean and colorless, achieving almost 100% decontamination of the dye pollutants (Fig. 4f). Our results collectively highlight that CB/PVDF@BFP is an efficient, interfacial photothermal steam generator for sustainable seawater desalination and wastewater treatment.

We have further assessed the cyclability/reversibility of our device in terms of its energy efficiency, amount of desalination water, open circuit voltage (V_{OC}) and short circuit current (I_{SC}; Fig. S20†). Throughout the five successive tests (Fig. S20a and b†), we observe that key figures of merits including evaporation rate, energy efficiency, and the amount of desalinated water collected from our device (size: 70 × 30 mm^2) remain relatively constant at ~1.41–1.49 kg m^{-2} h^{-1} (mean square deviation: ±1.8%), 92–96%, and 2.9–3.1 g, respectively, under one sun irradiation (50 RH% and 25 °C). These findings thus highlight the excellent reusability of our device which is an important criterion for long-term device application. Moreover, we also note that the trends for voltage and current outputs from our device are largely similar across five cyclability tests (Fig. S20c†). For instance, CB/PVDF@BFP yields an initial high V_{OC} of ~0.42 V which gradually declines to ~0.32 V after 60 min. Likewise, CB/PVDF@BFP also affords an initial I_{SC} of 2.3 μA which gradually stabilizes at 1.7 μA after 60 min. These current and voltage trends are also observed for subsequent test cycles.

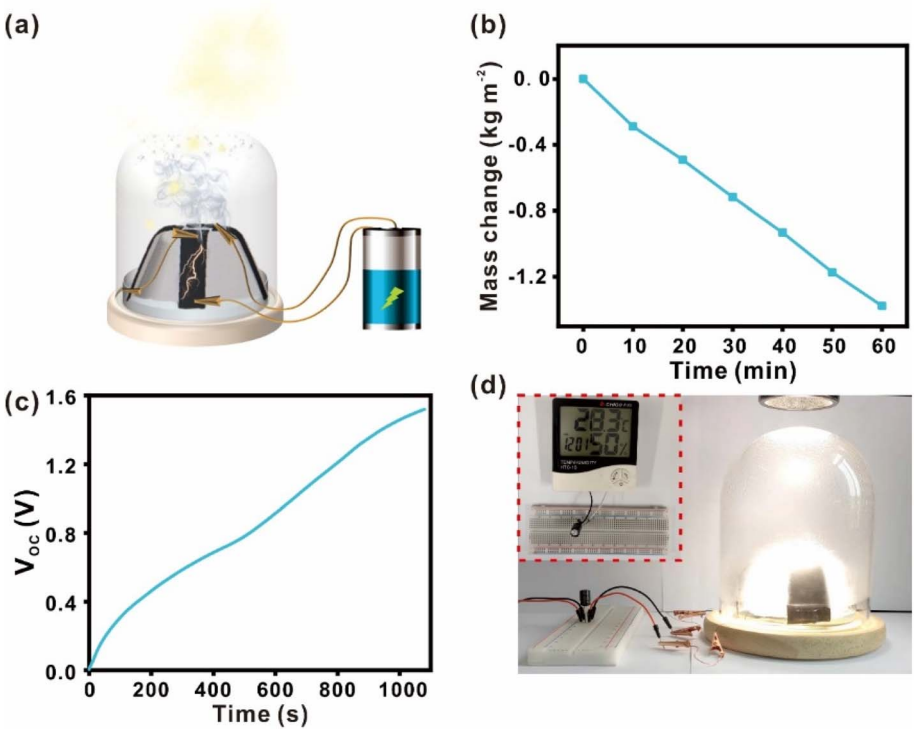

Fig. 5 Design and characterization of a dual-functional CB/PVDF@BFP-based device for concurrent solar-driven water purification and evaporation-induced electricity generation. (a) Scheme depicting the dual-functional device for concurrent production of clean water and green electricity. (b) Water evaporation rates using the dual-functional device under 1 sun irradiation and 25 °C. (c) V_{OC} of four CB/PVDF@BFP platforms connected in series. The electrical output is stored in a capacitor (50 V, 100 μF). (d) Application of the dual-functional device to power a small electronic device and to produce clean water.

Clearly, the consistent V_{OC} and I_{SC} output signifies that our device possesses efficient power generation stability over 5 repeated cycles (Fig. S20d†). Our results collectively emphasize the excellent reversibility of our unique design for simultaneous water purification and power generation processes.

Thus far, we have separately studied the CB/PVDF@BFP platform for its water evaporation and evaporation-induced power generation performances. To effectively combine these two complementary phenomena into an integrated process, we have built a dual-functional device to realize concurrent solar-driven steam generation and evaporation-induced power generation (Fig. 5a). In this experimental set-up, four CB/PVDF@BFP platforms are connected in series and placed within a glass dome to form the dual-functional device. Interestingly, we note that the bifunctional device yields a higher and more consistent water evaporation rate of ~1.377 kg m^{-2} h^{-1} over a prolonged duration of 1 h under similar one sun irradiation (Fig. 5b). This is attributed to the three-dimensional design of the bifunctional device which promotes sunlight absorption and subsequent water evaporation. The steam generated can be subsequently collected as clean water by condensation on the glass dome. Notably, the device undergoes simultaneous evaporation-induced power generation to reach a V_{OC} of 2.1 V using artificial seawater (3.5% salt; Fig. S21†). We also note that the maximum power generated is 306 nW when the load resistance is 2 MΩ (Fig. S18(b)†). The electrical power generated can be easily stored by charging a 10 MF capacitor to >1.5 V within 15 min (Fig. 5c), and be subsequently released on demand to power small household appliances (Fig. 5d), such as an LED lamp (1.5 V) or an LCD temperature display.

4. Conclusions

In conclusion, we have successfully fabricated a CB/PVDF@BFP platform for low-grade heat harvesting and applied it as a dual-functional device for concurrent solar-driven water evaporation and evaporation-induced power generation. Our strategy employs an asymmetric double-layer structure with an upper hydrophobic CB/PVDF layer for photothermal conversion, and a lower BFP layer for rapid water uptake and transfer to boost water evaporation. Notably, the designed platform is fabricated using a spray process which effectively integrates the two layers with no gap to promote water and heat transfer. The obtained bifunctional device provides rapid water evaporation and evaporation efficiency of 1.44 kg m^{-2} h^{-1} and 92%, respectively, under 1 kW m^{-2} of solar irradiation. The superior photothermal steam generation enables efficient seawater desalination and contaminated water purification with up to 99.8% and nearly 100% efficiency, respectively. At the same time, the device harnesses energy from the evaporation process and generates stable electrical outputs with a V_{OC} and I_{SC} of 0.32 V and 1.5 μA, respectively. The electrical output can be easily stored by charging a capacitor to 1.5 V within 15 min, and can be discharged to power small household electronics on demand. By enabling the parallel production of clean water and green energy, our work offers valuable insights for the efficient design of decentralized, multifunctional devices to tackle the energy and water crises using sunlight as a renewable energy source. This ensemble of benefits is crucial to address the sustainability issues faced by mankind, especially in remote areas with no access to the electricity grid and/or potable water. Our work shows that the dual-function device is a promising approach for the powering of low-power electronic equipment, seawater desalination and wastewater purification by collecting low-grade thermal energy.

Conflicts of interest

The authors declare no competing financial interest.

Acknowledgements

The authors gratefully acknowledge the financial support from the National Natural Science Foundation of China (21922202, 21673202 and 22073080), Natural Science Foundation of the Jiangsu Higher Education Institutions of China (21KJB430049) and Scientific research and practical innovation program (SJCX21_1569;2021-06-11). H. K. L. acknowledges the funding support from the Singapore Ministry of Education (AcRF Tier 1 RS13/20 and RG4/21), A*STAR Singapore (AME YIRG A2084c0158), National University of Singapore Center of Hydrogen Innovation (CHI-P2022-05), and Nanyang Technological University start-up grants.

References

1 A.-H. Cavusoglu, X. Chen, P. Gentine and O. Sahin, *Nat. Commun.*, 2017, **8**, 1–9.
2 A. Deshmukh, C. Boo, V. Karanikola, S. Lin, A. P. Straub, T. Tong, D. M. Warsinger and M. Elimelech, *Energy Environ. Sci.*, 2018, **11**, 1177–1196.
3 N. Xu, P. Zhu, Y. Sheng, L. Zhou, X. Li, H. Tan, S. Zhu and J. Zhu, *Joule*, 2020, **4**, 347–358.
4 C. Liu, K. Hong, X. Sun, A. Natan, P. Luan, Y. Yang and H. Zhu, *J. Mater. Chem. A*, 2020, **8**, 12323–12333.
5 Y. Xi, C. Du, P. Li, X. Zhou, C. Zhou and S. Yang, *Ind. Eng. Chem. Res.*, 2022, **61**, 4579–4587.
6 Z. Yu, R. Gu, Y. Tian, P. Xie, B. Jin and S. Cheng, *Adv. Funct. Mater.*, 2022, **32**, 2108586.
7 Y. Huang, H. Cheng, C. Yang, H. Yao, C. Li and L. Qu, *Energy Environ. Sci.*, 2019, **12**, 1848–1856.
8 H. Li, X. Li, X. Li, H. Wang, J. Huang, S. K. Boong, H. K. Lee, J. Han and R. Guo, *Nano Energy*, 2022, **99**, 107378.
9 H. Li, H. Wang, X. Li, J. Huang, X. Li, S. K. Boong, H. K. Lee, J. Han and R. Guo, *Nano Energy*, 2022, **100**, 107527.
10 S. Lv, W. He, Z. Hu, M. Liu, M. Qin, S. Shen and W. Gong, *Energy Convers. Manage.*, 2019, **196**, 69–76.
11 H. Ghasemi, G. Ni, A. M. Marconnet, J. Loomis, S. Yerci, N. Miljkovic and G. Chen, *Nat. Commun.*, 2014, **5**, 1–7.
12 T. G. Yun, J. Bae, A. Rothschild and I.-D. Kim, *ACS Nano*, 2019, **13**, 12703–12709.
13 T. Ding and G. W. Ho, *Joule*, 2021, **5**, 1639–1641.
14 T. Ding, Y. Zhou, W. L. Ong and G. W. Ho, *Mater. Today*, 2021, **42**, 178–191.

15 S. Cao, X. Wu, Y. Zhu, P. Gupta, A. Martinez, Y. Zhang, D. Ghim, Y. Wang, L. Liu, Y.-S. Jun and S. Singamaneni, *Adv. Energy Mater.*, 2021, **9**, 22585–22596.
16 Z. Liu, H. Song, D. Ji, C. Li, A. Cheney, Y. Liu, N. Zhang, X. Zeng, B. Chen and J. Gao, *Global Challenges*, 2017, **1**, 1600003.
17 W. Xu, X. Hu, S. Zhuang, Y. Wang, X. Li, L. Zhou, S. Zhu and J. Zhu, *Adv. Energy Mater.*, 2018, **8**, 1702884.
18 S. S. Das, V. M. Pedireddi, A. Bandopadhyay, P. Saha and S. Chakraborty, *Nano Lett.*, 2019, **19**, 7191–7200.
19 J. Li, K. Liu, G. Xue, T. Ding, P. Yang, Q. Chen, Y. Shen, S. Li, G. Feng and A. Shen, *Nano Energy*, 2018, **48**, 211–216.
20 G. Xue, Y. Xu, T. Ding, J. Li, J. Yin, W. Fei, Y. Cao, J. Yu, L. Yuan and L. Gong, *Nat. Nanotechnol.*, 2017, **12**, 317–321.
21 G. Chen, J. Sun, Q. Peng, Q. Sun, G. Wang, Y. Cai, X. Gu, Z. Shuai and B. Z. Tang, *Adv. Mater.*, 2020, **32**, 1908537.
22 M. Gao, C. K. Peh, H. T. Phan, L. Zhu and G. W. Ho, *Adv. Energy Mater.*, 2018, **8**, 1800711.
23 J. Liu, H. Yang, K. Liu, R. Miao and Y. Fang, *ChemSusChem*, 2020, **13**, 749–755.
24 Y. Yang, R. Zhao, T. Zhang, K. Zhao, P. Xiao, Y. Ma, P. M. Ajayan, G. Shi and Y. Chen, *ACS Nano*, 2018, **12**, 829–835.
25 H. Lin, B. C. Sturmberg, K.-T. Lin, Y. Yang, X. Zheng, T. K. Chong, C. M. de Sterke and B. Jia, *Nat. Photonics*, 2019, **13**, 270–276.
26 H. Ren, M. Tang, B. Guan, K. Wang, J. Yang, F. Wang, M. Wang, J. Shan, Z. Chen and D. Wei, *Adv. Mater.*, 2017, **29**, 1702590.
27 X. Zhou, F. Zhao, Y. Guo, Y. Zhang and G. Yu, *Energy Environ. Sci.*, 2018, **11**, 1985–1992.
28 S. He, C. Chen, Y. Kuang, R. Mi, Y. Liu, Y. Pei, W. Kong, W. Gan, H. Xie and E. Hitz, *Energy Environ. Sci.*, 2019, **12**, 1558–1567.
29 Y. Li, T. Gao, Z. Yang, C. Chen, W. Luo, J. Song, E. Hitz, C. Jia, Y. Zhou and B. Liu, *Adv. Mater.*, 2017, **29**, 1700981.
30 P. Zhang, J. Li, L. Lv, Y. Zhao and L. Qu, *ACS Nano*, 2017, **11**, 5087–5093.
31 L. Zhou, Y. Tan, D. Ji, B. Zhu, P. Zhang, J. Xu, Q. Gan, Z. Yu and J. Zhu, *Sci. Adv.*, 2016, **2**, e1501227.
32 M. Aizudin, R. Goei, A. J. Ong, Y. Z. Tan, S. K. Lua, R. P. Pottammel, H. Geng, X.-L. Wu, A. L. Y. Tok and E. H. Ang, *J. Mater. Chem. A*, 2022, **10**, 19612–19617.
33 Y. Lu, D. Fan, Y. Wang, H. Xu, C. Lu and X. Yang, *ACS Nano*, 2021, **15**, 10366–10376.
34 Y. Zhou, Q. Lu, Q. Liu, H. Yang, J. Liu, J. Zhuang, W. Shi and X. Wang, *Adv. Funct. Mater.*, 2022, **32**, 2112159.
35 J. Li, K. Liu, T. Ding, P. Yang, J. Duan and J. Zhou, *Nano Energy*, 2019, **58**, 797–802.
36 Z. Sun, L. Feng, X. Wen, L. Wang, X. Qin and J. Yu, *ACS Appl. Mater. Interfaces*, 2021, **13**, 56226–56232.
37 T. Tabrizizadeh, J. Wang, R. Kumar, S. Chaurasia, K. Stamplecoskie and G. Liu, *ACS Appl. Mater. Interfaces*, 2021, **13**, 50900–50910.
38 H. Li, J. Huang, H. Wang, X. Li, H. K. Lee, J. Han and R. Guo, *ACS Appl. Nano Mater.*, 2022, **5**, 2429–2435.
39 L. Li, M. Hao, X. Yang, F. Sun, Y. Bai, H. Ding, S. Wang and T. Zhang, *Nano Energy*, 2020, **72**, 104663.
40 J. Chi, C. Liu, L. Che, D. Li, K. Fan, Q. Li, W. Yang, L. Dong, G. Wang and Z. L. Wang, *Adv. Sci.*, 2022, **9**, 2201586.
41 X. Hu, W. Xu, L. Zhou, Y. Tan, Y. Wang, S. Zhu and J. Zhu, *Adv. Mater.*, 2017, **29**, 1604031.
42 S. Liu, C. Huang, X. Luo and Z. Rao, *Appl. Therm. Eng.*, 2018, **142**, 566–572.
43 Y. Wang, C. Wang, X. Song, S. K. Megarajan and H. Jiang, *J. Mater. Chem. A*, 2018, **6**, 963–971.
44 M. Xie, J. Qian, Y. Li, H. Yang, J. Qu, X. Hu and Q. Mao, *Appl. Opt.*, 2021, **60**, 4930–4937.
45 G. Xue, K. Liu, Q. Chen, P. Yang, J. Li, T. Ding, J. Duan, B. Qi and J. Zhou, *ACS Appl. Mater. Interfaces*, 2017, **9**, 15052–15057.